Vignette and Exposure Calibration and Compensation

Dan B Goldman and Jiun-Hung Chen
University of Washington

Figure 1 On the left, a panoramic sequence of images showing vignetting artifacts. Note the change in brightness at the edge of each image. Although the effect is visually subtle, this brightness change corresponds to a 20% drop in image intensity from the center to the corner of each image. On the right, the same sequence after vignetting is removed.

Abstract

We discuss calibration and removal of "vignetting" (radial falloff) and exposure (gain) variations from sequences of images. Unique solutions for vignetting, exposure and scene radiances are possible when the response curve is known. When the response curve is unknown, an exponential ambiguity prevents us from recovering these parameters uniquely. However, the vignetting and exposure variations can nonetheless be removed from the images without resolving this ambiguity. Applications include panoramic image mosaics, photometry for material reconstruction, image-based rendering, and preprocessing for correlation-based vision algorithms.

1. Introduction

Photographed images generally exhibit a radial falloff of intensity from the center of the image. This effect is known as "vignetting". Although lens manufacturers attempt to design their lenses so as to minimize the effects of vignetting, it is still present to some degree in all lenses, and can be quite severe for some aperture and focal length settings. We have found that at their maximum aperture settings, even high-quality fixed focal length lenses transmit 30% to 40% less light at the corners of an image than at its center. Zoom lenses and wideangle lenses for rangefinder cameras can exhibit even more severe vignetting artifacts.

Vignetting presents problems for a wide variety of applications. It affects graphics applications in which sequences of images are combined or blended, such as image-based rendering, texture projection and panoramic image mosaics; measurement applications in which radiometric quantities are estimated from images, such as material or lighting estimation; and vision applications in which brightness constancy is assumed for recovering scene structure, such as stereo correlation and optical flow. Yet despite its occurrence in essentially all photographed images, and its detrimental effect on these algorithms and systems, relatively little attention has been paid to calibrating and correcting vignette artifacts.

As we demonstrate, vignetting can be corrected easily using sequences of natural images without special calibration objects or lighting. Our approach can be used even for existing panoramic image sequences in which nothing is known about the camera. Figure 1 shows a series of aligned images, exhibiting noticeable brightness change along the boundaries of the images, even though the exposure of each image is identical. On the right, the same series of images is shown with vignetting removed using our algorithm.

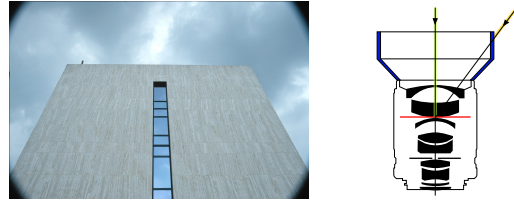The sources of vignetting can be classified according to the following four sources:[1]

Natural vignetting refers to radial falloff due to geometric optics: Different regions of the image plane receive different irradiance (see Figure 2). For simple lenses, these effects are sometimes modeled as a falloff of $\cos^4(\theta)$, where θ is the angle at which the light exits from the rear of the lens. Note that in all lenses, the distance from the exit pupil to the image plane changes when the focus distance is changed, so this component varies with focus distance. The $\cos^4$ law is only an approximation, which does not model real cameras and lenses well [24].

Pixel vignetting refers to radial falloff due to the angular sensitivity of digital optics. This type of vignetting – which affects only digital cameras – is due to the finite depth of the photon wells in digital sensors, which causes light striking a photon well at a steeper angle to be partially occluded by the sides of the well.

---

[1] We have used the terminology of Ray [20] and van Walree [24], but the definition of pixel vignetting is taken from Wikipedia [25], which uses a slightly different classification of the other types.
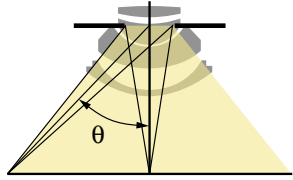
Figure 2 Illustration of the $\cos^4$ law. Points at the edge of the image plane receive less light than points at the center, due to inverse square falloff, Lambert's law, and foreshortening of the exit pupil. Carl Zeiss Planar 1.4/50 diagram by Mikhail Konovalov (c) Paul van Walree.

Figure 3 Left: image of a wall at f/1.4. Middle: same wall at f/5.6, showing that optical vignetting decreases with aperture size. Right: the shape of the entrance pupil varies with both the aperture (*x* axis) and the angle of incidence (*y* axis). The white openings correspond to the clear aperture for light that reaches the image plane. (c) Paul van Walree.

Optical vignetting refers to radial falloff due to light paths blocked inside the lens body by the lens diaphragm. It is also known as artificial or physical vignetting. This is easily observed by the changing shape of the clear aperture of the lens as it is viewed from different angles (see Figure 3), which reduces the amount of light reaching the image plane. Optical vignetting is a function of aperture width: It can be reduced by stopping down the aperture, since a smaller aperture limits light paths equally at the center and edges of frame.

Some lens manufacturers [26] provide relative illuminance charts that describe the compound effects of natural and optical vignetting for a fixed setting of each lens.

Mechanical vignetting refers to radial falloff due to certain light paths becoming blocked by other camera elements, generally filters or hoods attached to the front of the lens body (see Figure 4).

In the remainder of this work we will use the term "vignetting" to refer to radial falloff from any of these sources.

Because vignetting has many causes, it is difficult to predict the extent of vignetting for a given lens and settings. But, in general, vignetting increases with aperture and decreases with focal length. We have observed that the effect is often more visually prominent in film images than in digital images, probably due to the larger film plane and the steeper response curve.

Figure 4 The corners of the left image are blocked by a hood that is too long for the lens, as shown on the right. The lens is a Carl Zeiss Distagon 2/28, diagram by Mikhail Konovalov (c) Paul van Walree.

2. Related Work

Existing techniques for calibrating the vignetting effect typically require special equipment or lighting conditions. For example, Stumpfel *et al.* [22] acquire numerous images of a known illuminant at different locations in the image field and fit a polynomial to the acquired irradiances. In astronomy, related techniques are known as flat-field correction [17]. Kang and Weiss [13] have explored calibrating camera intrinsics using a simplified model of the vignetting effect, albeit with limited success.

Other researchers have simply attempted to detect vignettes [18], but do not attempt to model their form or correct their effects.

Schechner and Nayar [21] utilized a spatially varying filter on a rotating camera to capture high dynamic range intensity values. They calibrate this artificially-constructed spatial variation – which they call "intended vignetting" – using a linear least-squares fit. Our methods are a generalization of this approach in which exposures may vary between frames, and the response curve is not known in advance.

The effects of gain variation are widely known in the motion estimation literature. Altunbasak [3] uses a simple $\cos^4$ model of vignetting to compensate for spatial and temporal gain variation across an image sequence with known camera response. Candocia [6] developed a method to compensate for temporal exposure variation under unknown camera response, without reconstructing the absolute response or intensity values. More recently, Jia and Tang [12] have described a tensor voting scheme for correcting images with both global (gain) and local (vignetting) intensity variation.

Concurrent with our research, Litvinov and Schechner [15, 16] have developed an alternate solution to the same problem. Their approach applies a linear least squares solution in the log domain, using regularization in order to constrain response and spatial variation, as opposed to our use of parametric models.

3. Model and Assumptions

We will assume that the vignetting is radially symmetric about the center of the image, so that the falloff can be pa-

rameterized by radius r. We define the vignetting function, denoted $M(r)$, such that $M(0) = 1$ at the center.

We also assume that in a given sequence of images, vignetting is the same in each image. On SLR cameras this can be ensured by shooting in Manual or Aperture Priority mode, with a fixed focal length and focus distance, so that the geometry of the lens remains fixed over all frames.

We will also assume that the exiting radiance of a given scene point in the direction of the camera is the same for each image. This assumption will hold for all Lambertian scenes under fixed illumination, in which the radiance is constant over all directions. It also holds for non-Lambertian scenes under fixed illumination such that all frames share the same center of perspective. In the latter case, all images share the same ray exiting from a scene point, so the radiance does not change between frames.

Under these assumptions, we can model the pixel color $P_{\mathbf{x},i}$ of a scene point $\mathbf{x}$ as seen in frame i as

$$P_{\mathbf{x},i} = R(t_i L_{\mathbf{x}} M(r_{\mathbf{x},i})), \quad (1)$$

where R is the camera response curve, M is the vignetting function, t_i is the exposure (shutter duration) of frame i, $L_{\mathbf{x}}$ is the radiance of the point in the direction of the camera, and $r_{\mathbf{x},i}$ is the distance of the projection of $\mathbf{x}$ in image i from the optical center of the frame.

In portions of this work we will use parameterized models for M and R. We will use the notation M_α and R_β to refer to instances of these models with specific parameter vectors α and β, respectively.

4. Auto-Calibration

In this section we will discuss our methods for calibrating vignetting when the scene radiances are unknown and arbitrary (but are held fixed over all frames).

4.1. Known Response

If the response curve is known, we can recover high dynamic range pixel irradiances using multiple exposures of the same image. However, this may be time-consuming in practice: Even high-end cameras with automatic bracketing features will generally only provide at most two additional exposures on either side of the principal exposure. Instead, we make use of a small range of pixel exposures due to vignetting and camera exposure compensation. To accomplish this, we optimize the nonlinear objective function

$$Q_d(\alpha, t_i, L_{\mathbf{x}}) = \sum_{\mathbf{x},i} d\left[P_{\mathbf{x},i}, R(t_i L_{\mathbf{x}} M_\alpha(r_{\mathbf{x},i}))\right] \quad (2)$$

where $d[x,y]$ is a distance metric.

Note that we can only solve for the unknowns up to a scale ambiguity between the exposures t_i and radiances $L_{\mathbf{x}}$. We make the solution unique by choosing a particular frame

as the "reference" frame such that $t_0 = 1$. Our approach to minimizing Equation 2 is discussed in Section 6.

Schechner and Nayar [21] solved a linear version of this objective function, in which the response curve is inverted and the probability distribution of the recovered intensity is modeled as a Gaussian. Our approach differs mainly for saturated or nearly saturated pixels: In the linear approach, the covariance of the Gaussian becomes infinite and these pixels are effectively discarded in the optimization. In constrast, our approach retains saturated pixels as useful information, because they constrain the incoming radiance to be above the well-exposed range of intensities. In addition, we also recover the exposure of each frame.

4.2. Unknown Response

We now pose the following question: Can the vignetting function be recovered when the response curve is also unknown? Consider the objective function

$$Q_d(\alpha, \beta, t_i, L_{\mathbf{x}}) = \sum_{\mathbf{x},i} d\left[P_{\mathbf{x},i}, R_\beta\left(t_i L_{\mathbf{x}} M_\alpha(r_{\mathbf{x},i})\right)\right] \quad (3)$$

This objective function does not have a unique minimizer, even when we fix some values to account for the scale ambiguity mentioned in Section 4.1. We can easily demonstrate the existence of a family of scenes that produce exactly the same pixel values, and therefore will all produce the same value of Q. The construction of this family, parameterized by γ, is as follows:

If $P_{\mathbf{x},i} = R(t_i L_{\mathbf{x}} M(r_{\mathbf{x},i}))$, then let

$$R'(E_{\mathbf{x},i}) = R(E_{\mathbf{x},i}^{1/\gamma}) \quad (4)$$
$$t_i' = t_i^\gamma \quad (5)$$
$$L_{\mathbf{x}}' = L_{\mathbf{x}}^\gamma \quad (6)$$
$$M'(r_{\mathbf{x},i}) = M(r_{\mathbf{x},i})^\gamma \quad (7)$$

Therefore,

$$R'(t_i' L_{\mathbf{x}}' M'(r_{\mathbf{x},i})) = R(t_i L_{\mathbf{x}} M(r_{\mathbf{x},i})) \quad (8)$$

This construction defines a family of scene parameters (response curve, exposure, radiance, and vignetting) that all produce exactly the same images. Therefore, it is not possible to uniquely solve for a vignetting function when the response curve is unknown, without applying additional constraints.[2]

However, since this family of scene parameters all generate the same image pixels, it is possible to remove the vignetting effect *without* resolving either the γ-ambiguity or the scale ambiguity between t_i and $L_{\mathbf{x}}$. It suffices to find *any* solution in this family, remove the vignette, and regenerate

---

[2]Litvinov and Schechner [16] have suggested using entropy maximization to solve for γ.

new pixel values using our image formation model with the recovered parameters.

That is, the pixels generated by our imaging model with the vignette removed are the same for the entire family of optimal solutions. If the original pixel with vignetting is

$$
\begin{aligned}
P_{orig} &= R(t_i L_{\mathbf{x}} M(r_{\mathbf{x},i})) \\
&= R'(t_i' L_{\mathbf{x}}' M'(r_{\mathbf{x},i})),
\end{aligned} \tag{9}
$$

then we can generate new vignette-free pixel values as

$$
\begin{aligned}
P_{new} &= R'(t_i' L_{\mathbf{x}}') \\
&= R((t_i^\gamma L_{\mathbf{x}}^\gamma)^{1/\gamma}) \\
&= R(t_i L_{\mathbf{x}})
\end{aligned} \tag{10}
$$

This allows us to reconstruct vignette-free images without knowing the response curve in advance. We apply this mechanism in Section 6.3 to eliminate vignetting artifacts from panoramic mosaics.

5. Parameterizations and Algorithm

In this section we describe some of the specific parameterizations and techniques used to solve for and remove vignetting and exposure variations.

All our image sequences are pan-tilt sequences: multiple images that undergo no translation and only rotations about the center of perspective between frames. We assume that the scene is distant relative to the camera size, so that corresponding points on different images in this sequence receive the same radiance incident on the lens surface. This assumption allows us to infer that the differences in the intensity of corresponding pixels is due solely to lens and camera effects. Images were aligned using Brown and Lowe's Autostitch software [5, 4]. This method is robust to gain variations between images, so vignetting and exposure variation do not interfere with the spatial alignment.

Since we are modeling a compound effect from multiple sources, we use an approximate model of the radial falloff function. We have found that our ground truth images featuring optical and natural vignetting (Section 6.1) are well fit by parameterizing $M(r)$ as a 6th order even polynomial. We enforce the definition $M(0) = 1$ by holding the 0th order coefficient constant:

$$
M_\alpha(r) = 1 + \alpha_2 r^2 + \alpha_4 r^4 + \alpha_6 r^6. \tag{11}
$$

Although there is no unique minimizer to the objective function of Equation 3, we can use a model and prior that will provide a maximum *a priori* solution. Our model is the first 5 dimensions of the EMoR subspace [9], a PCA subspace that has been shown to represent a family of measured response curves well. Our prior is a Gaussian probability in this subspace. We estimate this Gaussian using the same database of response functions used to construct the EMoR model [8]. This is incorporated into the objective function of Equation 3 as an additional term, penalizing response curves that are far from the sample distribution with covariance Σ:

$$
Q(\alpha, \beta, t_i, L_{\mathbf{x}}) = Q_d(\alpha, \beta, t_i, L_{\mathbf{x}}) + \lambda Q_\Sigma(\beta), \tag{12}
$$

where λ controls the strength of the prior relative to the data term, and $Q_\Sigma(\beta) = \beta^T \Sigma^{-1} \beta$. The new term $Q_\Sigma(\beta)$ is thus proportional to the negative log likelihood of the Gaussian distribution.

How many constraints are necessary to solve our problem? When computing the solution, we need only consider points that are visible in more than one image. Each such point adds 2 or more constraints (depending on the number of images that include that point) and only 1 unknown. Our vignette model has 3 unknowns, the camera response model has 5 unknowns, and each of the N images has an unknown exposure value. Therefore, we need in theory only $8 + N$ points to compute a solution. However, we find in practice that due to image misalignment, noise, and the use of a polynomial basis for M – which is prone to extrapolation – many more points are needed for a robust solution. Each of the examples shown in this section used 1000-2000 points, sampled uniformly in a cylindrical coordinate system and projected into the individual images.

For color images, we make the simplifying assumption that all color channels have the same vignetting, response curve, and gain, but different intensity values $L_{\mathbf{x}}$. Thus each pixel provides three constraints.

To minimize Equations 2 and 3 we used an alternating optimization scheme, first fixing the parameters α, β and t_i while optimizing the $L_{\mathbf{x}}$, then fixing the $L_{\mathbf{x}}$ while optimizing parameters α, β and t_i. This exploits the dependency structure of the problem, in which the $L_{\mathbf{x}}$ depend on the other parameters but not upon each other, so that each subproblem solves for only a small number of parameters. Each subproblem optimizes the same objective function, taking a downhill step, and therefore the alternating optimization will converge.

We used the Nelder-Mead downhill simplex method [19] to solve each of the subproblems. The monotonicity constraint of the EMoR model is implemented as an infinite objective cost for values of β corresponding to non-monotonic response functions. We initialize the parameters as $\alpha = 0, \beta = 0, t_i = 1$, corresponding to no vignetting, mean response, and uniform exposure.

Since there are many $L_{\mathbf{x}}$ variables, their sub-optimization can be somewhat slow. We have accelerated this step by using a fast approximation in early iterations. In particular, we solve for $L_{\mathbf{x}}$ in Equation 1 and average the N observations:

$$
L_{\mathbf{x}} = \frac{1}{N} \sum_i \frac{R_\beta^{-1}(P_{\mathbf{x},i})}{t_i M_\alpha(r_{\mathbf{x},i})}, \tag{13}
$$

where N is the number of images overlapping sample $\mathbf{x}$. Then the full nonlinear objective function is evaluated using this approximate solution. If the energy is found to increase, the full nonlinear optimization is performed instead. Thus, in early iterations of the algorithm, we can take a fast downhill step without performing the full nonlinear optimization, postponing costly computations until later iterations. Our implementation – using Python's numarray module – took from 2 to 15 minutes to optimize parameters for the examples shown in Section 6, depending on the number of sample points and the amount of overlap between images.

We have experimented with both a squared distance metric and a robust thresholded error metric to compare pixel values. We have found in practice that the robust metric provides only a subtle improvement over squared distance, at a cost of significantly slower convergence. All of the results shown here therefore employed the squared distance metric, $d(P_1, P_2) = (P_1 - P_2)^2$.

6. Results

6.1. Reference Calibration

To obtain ground truth vignetting calibration, we apply a method inspired by that of Stumpfel *et al.* [22]. First, the response curve is recovered using multiple exposures [7]. Then, objects with fixed emissive properties are photographed at multiple spatial locations within the frame. We use a matte white card, taking care to avoid uneven lighting and specular reflections. Given the inverse response curve, the irradiance at a pixel is recovered from multiple exposures as $E_{\mathbf{x},i} = \frac{1}{N} \sum_i w_i R^{-1}(P_{\mathbf{x},i})/t_i$. The weighting w_i is chosen to downweight bright or dark pixels, for which the slope of R^{-1} is very high and the inverted values therefore have high variance.

We fit a polynomial vignetting function directly to the white card image by optimizing the following equation over all pixels:

$$Q(\alpha) = \sum_{\mathbf{x}} (E_{\mathbf{x},i} - M'_\alpha(r_{\mathbf{x},i}))^2 \tag{14}$$

where $M'_\alpha(r_{\mathbf{x},i}) = t_i L_0 M_\alpha(r_{\mathbf{x},i})$, and L_0 is the radiance of the reference object. The scale factor $t_i L_0$ is unknown, but we solve for α using the condition $M(0) = 1$.

Using this method, we obtained "ground truth" measurements and fit over a range of focal lengths, apertures, and focus distances. Our findings are summarized as relative illuminance charts in Figure 5. Each of these charts is normalized so that $M(0) = 1$ and the corners of the acquired image lie at $r_{\mathbf{x},i} = 1$.

Figures 5a) and 5b) illustrate reference calibration for a zoom lens. This lens exhibits significant vignetting across its entire range of focal lengths, but shorter focal lengths exhibit more significant vignetting. The vignetting is the same for most aperture settings, but at very wide apertures the effect of optical vignetting becomes more apparent.
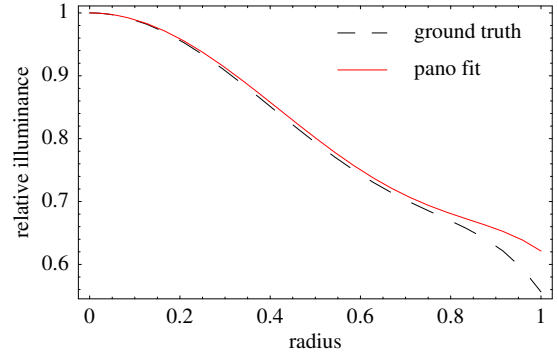
Figure 6 Comparison of our results to ground truth, for Canon EOS 10D, 28mm-135mm zoom at 28mm, f/3.5. Polynomial fit to ground truth in black dashes, our solution in solid red.

Figures 5c) and 5d) illustrate measurements for a fixed-focal length lens. Such lenses can generally be designed to mitigate image artifacts such as vignetting, because they have fewer optical elements. Indeed at smaller apertures the lens remains nearly vignette-free, but at apertures greater than f/4 and focus distances further than .5m, the vignetting becomes quite significant. At f/2.8, points at the corner of the image receive just 60% of the light received at the center.

6.2. Auto-Calibration with Known Response

To analyze the accuracy of our auto-calibration approach we acquired a panoramic sequence of images of a natural scene using the same lens and settings as one of our white card images from Section 6.1, and fit a vignetting function to the panoramic sequence by optimizing Equation 2 over 2000 points in the cylindrical coordinate system of the panorama. A comparison of vignette curves using the two methods is shown in Figure 6.

The fits are nearly identical, except toward the corners of the image ($r_{\mathbf{x},i} \to 1$) where fewer image samples constrain the fit.
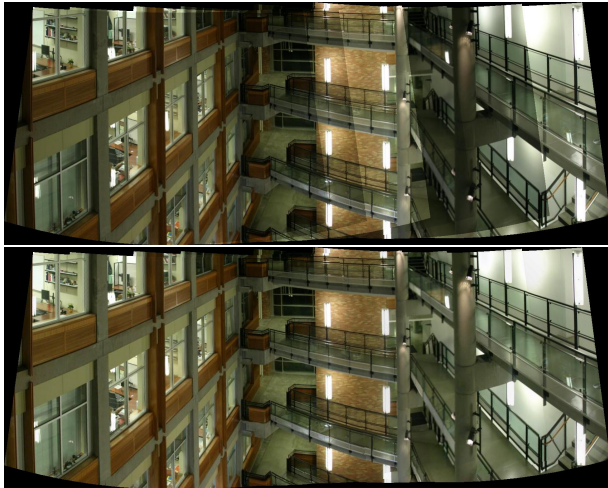
6.3. Vignette-Free Panoramic Mosaics

To reconstruct image sequences free of vignettes and exposure variation, we minimize Equation 3 (or Equation 2, if the response curve is previously calibrated) using a sampling of points chosen as described previously. We note that in an aperture-priority sequence, each image is exposed properly for its own field of view, but there may be no single image exposed at a level that represents the entire scene well. We therefore compute a new "ideal" exposure for the entire sequence using the geometric mean of the individual exposures:

$$t_{new} = \left(\prod_i t_i \right)^{1/N} \tag{15}$$
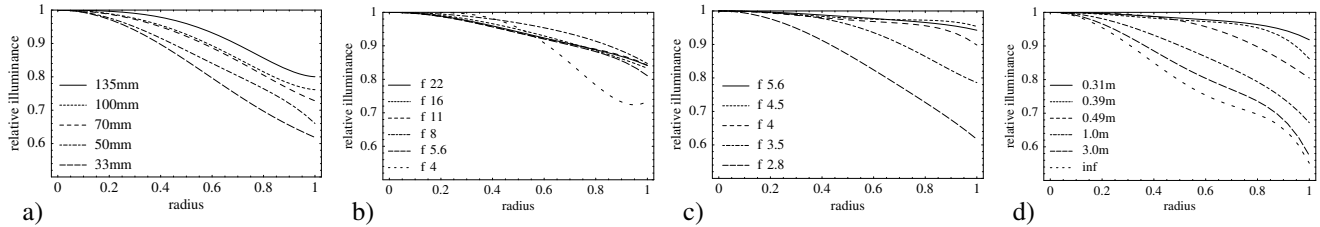
Figure 5 Relative illuminance charts. a) Canon 28mm-135mm zoom, multiple focal lengths. b) Canon 28mm-135mm zoom, multiple apertures. c) Canon 100mm, multiple apertures. d) Canon 100mm, multiple focus distances. For these lenses, falloff increases with aperture and focus distance, but decreases with focal length.

Figure 7 A panoramic mosaic using aperture-priority exposure, aligned and composited without blending. Above: original images. Below: after vignette and exposure compensation.

Figure 8 Foggy lake. From top: original images; original images after Photomontage blending; vignette compensation only; vignette compensation and Photomontage blending.

We now solve for the vignette-free exposure-compensated pixel values by inverting the image formation equation, dividing out the vignette and exposure variation, and reapplying the new ideal exposure and recovered response curve.

$$P_{\mathbf{x},i}^{new} = R_\beta \left(\frac{t_{new} R_\beta^{-1}(P_{\mathbf{x},i})}{M_\alpha(r_{\mathbf{x},i}) t_i} \right) \qquad (16)$$

Figure 7(top) shows a mosaic of images photographed in the camera's aperture priority mode with no compensation and no blending. Aperture priority means that each image has the same aperture but varying shutter duration, so that the exposure differs in each frame but not the vignetting. Figure 7(bottom) shows the same images with vignette and exposure compensation, and no blending. For this image, the response curve of this camera was separately calibrated [7]. Note that traditional panoramic mosaics are photographed using fixed exposure settings, whereas our method enables even aperture priority sequences such as this one to be stitched together as panoramas.

Although we cannot recover absolute or relative radiance values from images with unknown response curve, we demonstrate that vignettes and exposure variation can

nonetheless be removed from such images. Figure 8 is one such sequence, showing significant exposure variation and vignetting artifacts can be eliminated with our process. Figure 9 illustrates the same capability using a panoramic sequence of 12 images taken during the Apollo 11 mission in July 1969 [1, 23]. Reference calibration of this camera is presently impossible, as the camera and lens were left on the surface of the moon in order to minimize fuel consumption for the astronauts' return voyage. Despite the poor alignment of the images (probably due to parallax), our algorithm robustly compensates for almost all the brightness variation within and between the images.

Although our method aligns the color values of the multiple images in a panoramic sequence, it does not eliminate all edge artifacts. One reason is that the polynomial model
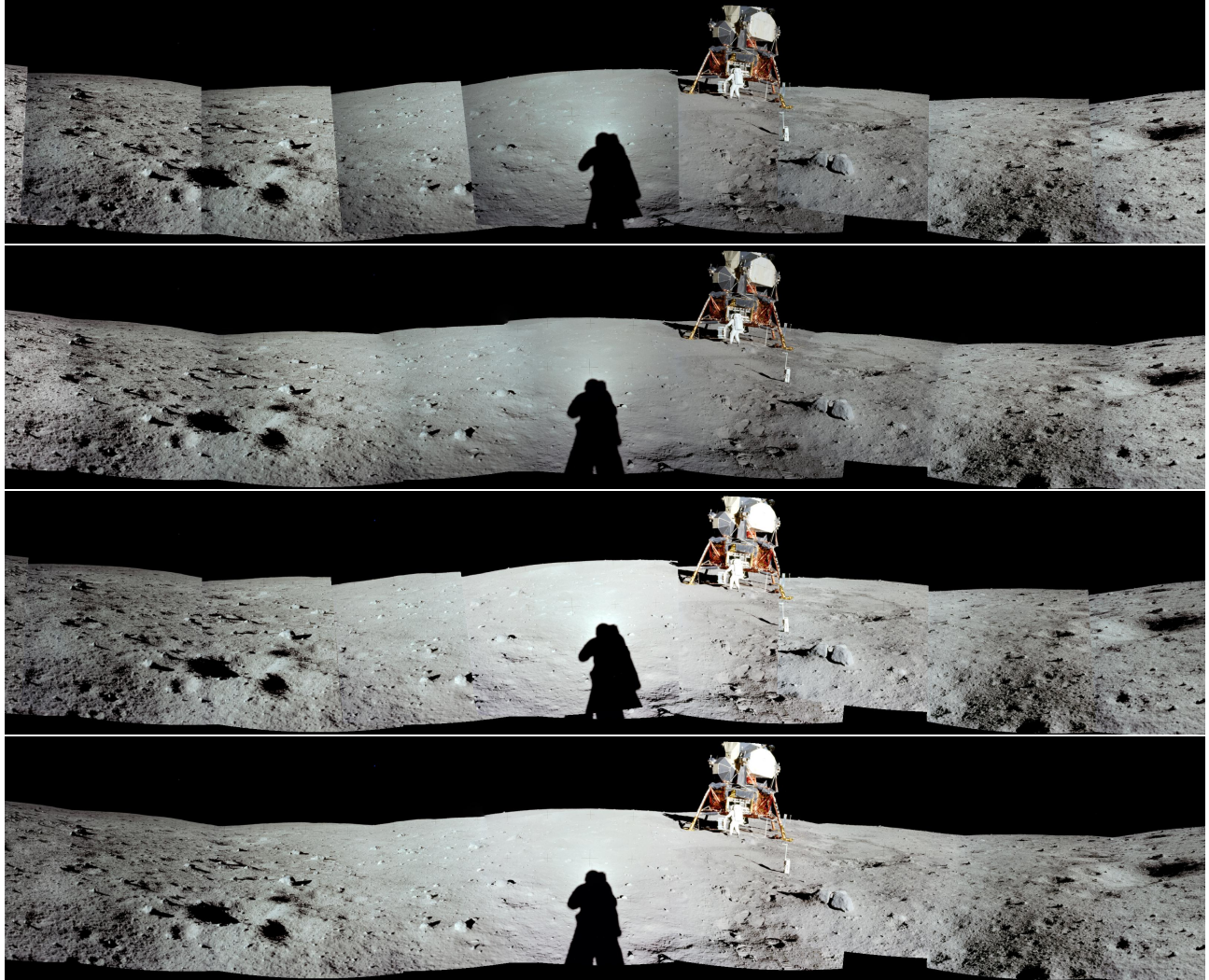
Figure 9 Apollo 11. From top: original images; original images after Photomontage blending; vignette compensation only; vignette compensation and Photomontage blending.

for vignetting does not accurately represent all sources of radial falloff, and also extrapolates poorly towards the corners of images where the samples are sparser. These remaining artifacts can generally be removed using image blending methods.

However, we consider blending to be orthogonal to vignette and exposure compensation, as blending alone does not alleviate vignetting or exposure artifacts. To demonstrate this effect, we applied the Photomontage method of Agarwala et al. [2], which identifies optimal seams between images using graph cuts, then blends the images using gradient-domain fusion [14]. Without vignette or exposure compensation, strange shadows and low-frequency intensity oscillations can be seen in the composite image (see right side of top 2 images in Figure 8). However, with vignette and exposure compensation, the seams between images are already nearly invisible even before blending (3rd from top).

Note that after exposure and vignette compensation, the surface of the moon in Figure 9 appears brighter in the direction opposite the sun (near the photographers' shadows, in the center of the image) than in the direction towards the sun. This is not an artifact of the algorithm, but a manifestation of the high retroreflectivity of the moon's surface [10, 11]. The variation in brightness can also be inferred indirectly by examining the gradients of filtered versions of the original images: The x component of the gradients point away from the sun in each image. This physical effect is observable only after vignette and exposure compensation.

7. Conclusion and Future Work

Vignetting is often ignored due to the perceived difficulty of calibration, but it is a significant effect even for high-end

cameras and lenses. We have shown that when the response curve is known, the vignetting function and exposure variations can be calibrated using corresponding points in multiple images. Such calibration is necessary to obtain accurate image radiometry, such as when estimating reflectance or incident illumination.

When the response curve is unknown, the vignetting function, image exposure, and scene radiance cannot be recovered uniquely. However, images can be reconstructed with uniform exposure and without vignettes using any of the family of solutions to an optimization. In addition to the demonstrated application to panoramic image mosaics, this type of vignette and exposure compensation can be utilized to improve the quality of image-based rendering, and also as a preprocessing step for a variety of vision algorithms which assume spatial and temporal invariance, such as BRDF measurement, photometric stereo, multiview stereo and optical flow.

Several areas for improvement remain. Our system presently requires multiple frames with the same vignetting function, implying the lens settings must be held fixed; We would like to be able to compensate for vignetting in arbitrary panoramic sequences, or even in a single frame. Both of these problems will likely require more sophisticated models for vignetting beyond our simple polynomial fit. We are also interested in methods to compensate for other artifacts seen in panoramic mosaics, such as variable color balance, glare, and lens flare.

Acknowledgements

References

[1] Hasselblad in Space. http://www.hasselblad.se/general/listWithItems.asp?secId=585.

[2] A. Agarwala, M. Dontcheva, M. Agrawala, S. Drucker, A. Colburn, B. Curless, D. Salesin, and M. Cohen. Interactive digital photomontage. *ACM Trans. Graphics (Proc. SIGGRAPH)*, 23(4):294–301, 2004.

[3] Y. Altunbasak, R. M. Mersereau, and A. J. Patti. A fast parametric motion estimation algorithm with illumination and lens distortion correction. *IEEE Trans. Image Proc.*, 12(4):395–408, 2003.

[4] M. Brown and D. Lowe. Autostitch home page. http://www.autostitch.net, 2005.

[5] M. Brown and D. G. Lowe. Recognising panoramas. In *Proc. ICCV*, pages 1218–1225, 2003.

[6] F. M. Candocia. Jointly registering images in domain and range by piecewise linear comparametric analysis. *IEEE Trans. Image Proc.*, 12(4):409–419, 2003.

[7] P. E. Debevec and J. Malik. Recovering high dynamic range radiance maps from photographs. In *Proc. SIGGRAPH*, volume 31, pages 369–378, 1997.

[8] M. D. Grossberg. DoRF and EMoR home page. http://www1.cs.columbia.edu/CAVE/research/softlib/dorfEmor.html.

[9] M. D. Grossberg and S. K. Nayar. What is the space of camera response functions? In *Proc. CVPR*, pages 602–609, 2003.

[10] B. Hapke. Optical properties of the lunar surface. In Kopal, editor, *Physics and astronomy of the Moon*. Academic Press, 1971.

[11] H. W. Jensen, F. Durand, M. Stark, S. Premoze, J. Dorsey, and P. Shirley. A physically-based night sky model. In *Proc. SIGGRAPH*, pages 399–408, Aug. 2001.

[12] J. Jia and C.-K. Tang. Tensor voting for image correction by global and local intensity alignment. *PAMI*, 27(1):36–50, 2005.

[13] S. B. Kang and R. Weiss. Can we calibrate a camera using an image of a flat textureless Lambertian surface? In *Proc. ECCV*, volume 2, pages 640–653, 2000.

[14] A. Levin, A. Zomet, S. Peleg, and Y. Weiss. Seamless image stitching in the gradient domain. In *Proc. ECCV*, volume 4, pages 377–389, 2004.

[15] A. Litvinov and Y. Y. Schechner. Addressing radiometric nonidealities: A unified framework. In *Proc. CVPR*, pages 52–59, 2005.

[16] A. Litvinov and Y. Y. Schechner. Radiometric framework for image mosaicking. *JOSA A*, 22(5):839–848, 2005.

[17] J. Manfroid. On CCD standard stars and flat-field calibration. *Astronomy and Astrophysics Supplement Series*, 118:391–395, Aug. 1996.

[18] T. Mitsunaga and S. K. Nayar. Radiometric self calibration. In *Proc. CVPR*, volume 1, pages 1374–1380, 1999.

[19] W. H. Press, S. A. Teukolsky, W. T. Vetterling, and B. P. Flannery. *Numerical Recipes in C: The Art of Scientific Computing (2nd ed.)*. Cambridge University Press, 1992.

[20] S. F. Ray. *Applied Photographic Optics*. Focal Press, 3rd edition, 2002.

[21] Y. Y. Schechner and S. K. Nayar. Generalized mosaicing: High dynamic range in a wide field of view. *IJCV*, 53(3):245–267, 2003.

[22] J. Stumpfel, A. Jones, A. Wenger, and P. Debevec. Direct HDR capture of the sun and sky. In *Proc. AfriGraph*, pages 145–149, 2004.

[23] K. Teague. The Project Apollo Image Gallery. http://www.apolloarchive.com/apollo_gallery.html, 2004.

[24] P. van Walree. Vignetting. http://www.vanwalree.com/optics/vignetting.html, 2004.

[25] Wikipedia: Vignetting. http://en.wikipedia.org/wiki/Vignetting, June 2005.

[26] Carl Zeiss International. http://www.zeiss.com, 2005.